New Journal of Physics
The open access journal at the forefront of physics

Deutsche Physikalische Gesellschaft DPG IOP Institute of Physics

Control of photoelectron momentum distributions by bichromatic polarization-shaped laser fields

New Journal of Physics
The open access journal at the forefront of physics

Deutsche Physikalische Gesellschaft DPG
IOP Institute of Physics

Published in partnership with: Deutsche Physikalische Gesellschaft and the Institute of Physics

OPEN ACCESS

RECEIVED
14 June 2017

REVISED
24 July 2017

ACCEPTED FOR PUBLICATION
2 August 2017

PUBLISHED
20 October 2017

PAPER

Control of photoelectron momentum distributions by bichromatic polarization-shaped laser fields

Stefanie Kerbstadt, Dominik Pengel, Daniela Johannmeyer, Lars Englert, Tim Bayer and Matthias Wollenhaupt

Carl von Ossietzky Universität Oldenburg, Institut für Physik, Carl-von-Ossietzky-Straße 9-11, D-26129 Oldenburg, Germany

E-mail: matthias.wollenhaupt@uni-oldenburg.de

Keywords: ultrafast polarization shaping, bichromatic laser fields, photoelectron imaging spectroscopy, tomographic reconstruction, free electron wave packets, resonance enhanced multi-photon ionization

Abstract

Bichromatic polarization-shaped femtosecond laser pulses are used to control three-dimensional photoelectron momentum distributions (3D-EDs) from resonance enhanced multi-photon ionization of potassium atoms. The light fields consisting of two spectral bands with different ellipticity are produced using an ultrafast polarization pulse shaper equipped with a custom polarizer in the Fourier plane. The tomographically reconstructed 3D-EDs from ionization with counterrotating circularly or orthogonal linearly polarized bichromatic laser pulses show different angular momentum superposition states at four distinct photoelectron energies. The analysis of the measured 3D-EDs reveals that the underlying physical mechanism is based on the interplay of ionization pathway selection via quantum mechanical selection rules for optical transitions and intrapulse frequency mixing of the spectral bands with different ellipticity.

1. Introduction

Femtosecond polarization pulse shaping [1–5] is an established experimental technique which provides access to the spatial nature of the light–matter interaction by control of the instantaneous ellipticity of the laser pulse. Control by polarization-shaped femtosecond laser pulses has been demonstrated in numerous experiments including coherent manipulation of two-photon absorption in atomic rubidium [6] and optimization of the ion yield in the multi-photon ionization of potassium dimers [7]. In addition, in [8] the extraction of a full set of ionization matrix elements from multi-photon ionization with polarization-shaped femtosecond laser pulses was demonstrated. Recently, ultrashort bichromatic laser fields with individual polarization state of each color have emerged as a powerful tool for coherent control of ultrafast electron dynamics in diverse applications comprising strong-field ionization of atoms [9–13], charge localization in ultrafast photochemical reactions [14, 15], and phase control of electric currents in semiconductors [16, 17] and metals [18]. In particular, in high-order harmonic generation (HHG) and HHG spectroscopy, polarization-shaped bichromatic fields are routinely employed to steer electron wave packets from tunneling ionization and control the rescattering process. The use of linearly polarized bichromatic driving fields permits the generation of even harmonics [19–21] and temporal shaping of the attosecond pulse train [20, 22–25]. The use of circularly polarized bichromatic driving fields leads to the emission of elliptically polarized harmonics, as proposed in [19, 26, 27] and demonstrated only recently [28–30]. In addition, bicircular HHG has been proposed as a technique to generate attosecond magnetic field pulses [31] and to extract spectroscopic information on atomic and molecular symmetries [32–34].

In this contribution, we demonstrate control of three-dimensional photoelectron momentum distributions (3D-EDs) from atomic resonance enhanced multi-photon ionization (REMPI) in the perturbative regime using bichromatic polarization-shaped femtosecond laser fields. Specifically, we study $1 + 2$ REMPI of potassium atoms with a sequence of counterrotating circularly polarized (CNR-CP) and orthogonal linearly polarized (O-LP) bichromatic femtosecond laser pulses. The use of bichromatic polarization-shaped pulses disentangles

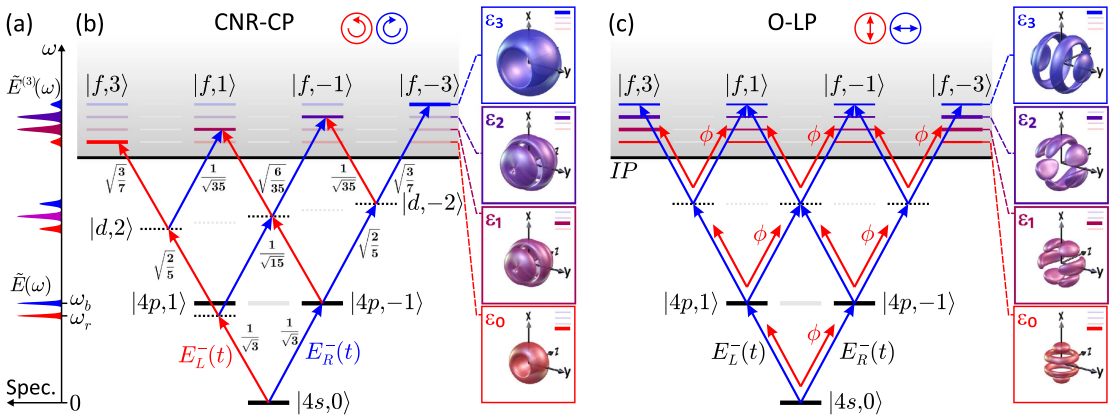

Figure 1. Scheme for three-photon ionization of potassium atoms with CNR-CP and O-LP bichromatic femtosecond laser pulses. (a) Fundamental spectrum $\tilde{E}(\omega)$ and resulting third order spectrum $\tilde{E}^{(3)}(\omega)$ of a linearly polarized bichromatic pulse with spectral bands centered at ω_r and ω_b. (b) The L-CP red pulse is described by $E_L^-(t)$, the R-CP blue pulse by $E_R^-(t)$. In the spherical basis, $E_L^-(t)$ exclusively drives $\Delta m = -1$ transitions, whereas $E_R^-(t)$ drives $\Delta m = +1$ transitions. (c) The *s*-polarized red and *p*-polarized blue pulse are both described by a superposition of an R-CP and an L-CP field in the spherical basis. Therefore, both pulses simultaneously drive $\Delta m = -1$ and $\Delta m = +1$ transitions. The 90° spatial rotation of the red pulse with respect to the blue introduces an optical phase of $\phi = \pi$ in the R-CP component of the red pulse. The insets show generic 3D-EDs corresponding to the free electron wave packets centered at $\varepsilon_0 \ldots \varepsilon_3$ in red, magenta, purple, and blue, respectively.

multiple ionization pathways by energetic separation of different angular momentum target states. Control of the ionization pathway along with energy- and angle-resolved detection allows us, on the one hand, to generate individual angular momentum free electron wave packets using CNR-CP bichromatic pulses and, on the other hand, to create unusual angular momentum superposition states using O-LP bichromatic pulses. In the experiment, bichromatic polarization-tailored fields are produced using a 4*f* polarization pulse shaper [35] equipped with a custom polarizer in the Fourier plane [36, 37]. Multiple photoelectron momentum images are recorded employing a velocity map imaging (VMI) spectrometer [38] and subsequently combined to reconstruct the 3D-EDs using a tomography algorithm [39–41]. Positive and negative time delays between the two colors are introduced to discriminate resonant from non-resonant ionization and to observe signatures from spin–orbit wave packets (SOWPs) in the 3D-EDs. A similar setup was recently used to produce electron vortices with a sequence of two one-color CNR-CP femtosecond laser pulses [42]. In that experiment, the minimal time delay in the sequence was given by the pulse length in order to avoid the creation of linear polarization in the overlapping interval. However, CNR-CP bichromatic fields, consisting of temporally overlapping left- (L-CP) and right-handed circularly (R-CP) polarized disjoined spectral bands do not create linearly polarized light. This feature allows us to observe photoelectrons from REMPI by overlapping bichromatic CNR-CP pulses such that frequency mixing between photons of opposite helicity can occur. For example, we demonstrate that 3D-EDs from three-photon ionization with two red L-CP photons and one blue R-CP photon are observed in a specific kinetic energy window.

We start in section 2 with a theoretical discussion of the 3D-EDs from $1 + 2$ REMPI with bichromatic polarization-shaped laser pulses. Section 3 introduces the experimental strategy based on the combination of polarization pulse shaping and tomographic photoelectron imaging. The experimental results for CNR-CP and O-LP pulses are presented in section 4.

2. Theory

A theoretical description of photoelectron distributions from multi-photon atomic ionization with polarization-shaped laser pulses has been presented in the context of designer electron wave packets [41] and highly multiplexed coherent quantum metrology [8]. Here, we consider REMPI of atoms using polarization-shaped bichromatic CNR-CP and O-LP femtosecond laser pulses. Due to the selection rules $\Delta l = \pm 1$ and $\Delta m = \pm 1$ for $\sigma^{\pm}$-transitions, polarization-shaped pulses give rise to numerous interfering ionization pathways. For simplicity, only pathways with $\Delta l = +1$ transitions are depicted in figure 1 and spin–orbit splittings are omitted. However, in our numerical simulations (see sections 4.1 and 4.2) all possible pathways are taken into account, according to the treatment described in [8], where the contribution of $\Delta l = -1$ transitions was studied in detail. For $\Delta l = +1$ transitions, three-photon ionization as displayed in figures 1(b) and (c) connects the 4*s* ground state to a continuum with an angular momentum of $l = 3$, i.e. an *f*-type continuum. The resulting free electron wave packet is composed of the angular momentum eigenstates $|f, m_j\rangle$ with

$m_j = +3, +1, -1$, and -3, weighted by the kinetic energy-dependent amplitudes $a_{m_j}(\varepsilon)$

$$|\psi(\varepsilon)\rangle \propto \sum_{j=0}^{3} a_{m_j}(\varepsilon)|f,\ m_j\rangle. \tag{1}$$

In general, the $a_{m_j}(\varepsilon)$ are determined by the shape of the ionizing laser pulse [39, 43] and describe the kinetic energy distribution of each angular momentum state $|f,\ m_j\rangle$. In the weak-field limit, these amplitudes can be calculated using third order time-dependent perturbation theory and are given by the coherent superposition of all ionization pathways that lead from the ground state $|4s,\ 0\rangle$ to the target states $|f,\ m_j\rangle$. For a complete description, the $4p$ resonance needs to be taken into account [8, 44–46]. In order to present a simple and intuitive physical picture however, we restrict the following analytical description to non-resonant multi-photon ionization. For ionization pathways proceeding exactly via the $4p$ resonance, e.g. pathway $|4s,\ 0\rangle \longrightarrow |4p,\ -1\rangle \longrightarrow |d,\ -2\rangle \longrightarrow |f,\ -3\rangle$ in figure 1(b), an additional resonant term arises. Generally, the interference between resonant and non-resonant contributions leads to an additional modulation of the photoelectron energy distribution [44] which is not captured in the analytical model presented below (but is considered in the numerical simulations). Some effects due to the resonance observed in the experimental data are discussed in sections 4.1 and 4.2. In the non-resonant case, each individual ionization pathway depicted in figure 1 maps the third order optical spectrum of the driving laser pulse onto the continuum [47], taking into account the helicity of the photons absorbed in each transition. We describe the polarization-shaped laser pulse by the (negative frequency) analytic signal of its electric field $\boldsymbol{E}^-(t)$ decomposed into an L-CP component $E_L^-(t)$ and an R-CP component $E_R^-(t)$, i.e. $\boldsymbol{E}^-(t) = E_L^-(t)\boldsymbol{e}_L + E_R^-(t)\boldsymbol{e}_R$, where $\boldsymbol{e}_{L/R}$ are the spherical basis vectors. Then, for example, the contribution from the ionization pathway $|4s,\ 0\rangle \xrightarrow{L} |4p,\ 1\rangle \xrightarrow{R} |d,\ 0\rangle \xrightarrow{L} |f,\ 1\rangle$ can be written as

$$a_{m_j=1}^{(LRL)}(\varepsilon) \propto R_{s,p,d,f}^{(3)} \cdot C^{0\,1\,1}_{0\,1\,1} \cdot C^{1\,1\,2}_{1\,-1\,0} \cdot C^{2\,1\,3}_{0\,1\,1} \int_{-\infty}^{\infty} E_L^-(t)E_R^-(t)E_L^-(t)\mathrm{e}^{\mathrm{i}\omega_\varepsilon t}\mathrm{d}t, \tag{2}$$

with the total electron energy $\hbar\omega_\varepsilon = \varepsilon + \mathrm{IP}$ being the sum of the kinetic excess energy ε and the atomic ionization potential IP. The prefactor $R_{s,p,d,f}^{(3)}$ in equation (2) describes the radial part of the three-photon transition dipole matrix element. The angular part is described by the product of three Clebsch–Gordan coefficients (CGCs) $C^{l_1\ 1\ l_2}_{m_1\ \Delta m\ m_2}$ reflecting the angular momentum coupling i.e. dipole selection rules. The time-integral describes the photoelectron kinetic energy distribution for this specific ionization pathway. Making use of the Fourier convolution theorem, this term is rewritten as

$$\begin{aligned}\tilde{E}_{LRL}^{(3)}(\omega_\varepsilon) &= \int_{-\infty}^{\infty} E_L^-(t)E_R^-(t)E_L^-(t)\mathrm{e}^{\mathrm{i}\omega_\varepsilon t}\mathrm{d}t \\ &= \frac{1}{4\pi^2}(\tilde{E}_L^- \otimes \tilde{E}_R^- \otimes \tilde{E}_L^-)(-\omega_\varepsilon).\end{aligned} \tag{3}$$

Herein, $\tilde{E}_q^-(\omega)$ $(q = L,\ R)$ is the Fourier transform of the corresponding temporal field $E_q^-(t)$ and '$\otimes$' denotes the convolution. In general, by associating q with the photon angular momentum, i.e. $q = 1$ for L-CP and $q = -1$ for R-CP light, the total amplitude $a_{m_j}(\varepsilon)$ in equation (1) can be expressed as

$$a_{m_j}(\varepsilon) \propto \sum_{\{q_1q_2q_3\}} C^{0\ 1\ 1}_{0\ q_1\ q_1} \cdot C^{1\ 1\ \ 2}_{q_1\ q_2\ (q_1+q_2)} \cdot C^{2\ \ 1\ 3}_{(q_1+q_2)\ q_3\ m_j} \cdot E_{q_1q_2q_3}^{(3)}(\omega_\varepsilon). \tag{4}$$

The sum runs over all helicity combinations $\{q_1q_2q_3\}$ with $q_1 + q_2 + q_3 = m_j$, that is all three-photon ionization pathways connecting the ground state $|4s,\ 0\rangle$ with a given continuum state $|f,\ m_j\rangle$. Equation (4) highlights the interplay between the dipole selection rules represented by the CGC products and frequency mixing reflected by the third order optical spectra.

So far, the discussion is valid for any polarization-shaped laser field. Now, we specifically consider a bichromatic laser pulse consisting of two, e.g., Gaussian-shaped spectral bands with central frequencies ω_r (red band) and $\omega_b > \omega_r$ (blue band) and individual ellipticities. In general, frequency mixing of both colors gives rise to four contributions to $\tilde{E}_{q_1q_2q_3}^{(3)}(\omega)$ centered at frequencies $\omega_n = (3-n)\,\omega_r + n\,\omega_b$, with $n = 0 \ldots 3$ (see figure 1(a)). As a consequence, the photoelectron amplitudes $a_{m_j}^{(q_1q_2q_3)}(\varepsilon)$ generally also exhibit four contributions centered at kinetic energies $\varepsilon_n = (3-n)\,\hbar\omega_r + n\,\hbar\omega_b - \mathrm{IP}$, $n = 0 \ldots 3$. However, CNR-CP excitation as shown in figure 1(b) provides a unique mapping between helicity and color of each photon. Therefore, in this specific case, each amplitude $a_{m_j}^{(q_1q_2q_3)}(\varepsilon)$ exhibits only a single contribution with central energy ε_n determined by the number of absorbed photons from each color. The relative weight a_{nj} of this contribution is completely determined by the corresponding CGCs. An overview of all coefficients a_{nj} and their decomposition into angular (CGC) and radial ($\tilde{E}_{q_1q_2q_3}^{(3)}$) part in the CNR-CP case is given in table 1. In contrast, for O-LP excitation as shown in figure 1(c) both colors are described by superpositions of an L-CP and an R-CP field. In turn, each field $E_q^-(t)$ has a bichromatic spectrum. Therefore, all frequency mixing pathways deliver a non-zero contribution to $\tilde{E}_{q_1q_2q_3}^{(3)}(\omega)$ and hence to the amplitudes $a_{m_j}^{(q_1q_2q_3)}(\varepsilon)$. The relative weights a_{nj} are determined by the

Table 1. (a) Coefficient matrix $\{a_{nj}\}$ for three-photon ionization of potassium atoms with CNR-CP bichromatic femtosecond laser pulses. (b) Decomposition of the contribution weights a_{nj} into a radial part determined by the energy distribution $\gamma(\varepsilon - \varepsilon_n)$ and an angular part given by the product of CGCs along the corresponding ionization pathway. Due to the unique mapping between helicity and color in the CNR-CP case, each energy window is associated with only one state $|f, m_j\rangle$, leading to a complete energetic disentanglement of the target states.

(a)

ε_n, $m_j =$	$+3$	$+1$	-1	-3
ε_3	0	0	0	1
ε_2	0	0	$\sqrt{\frac{3}{5}}$	0
ε_1	0	$\sqrt{\frac{3}{5}}$	0	0
ε_0	1	0	0	0

(b)

m_j	$+3$	$+1$	-1	-3
$\lvert c_n^{(q_1q_2q_3)}\rvert$	1	1	1	1
	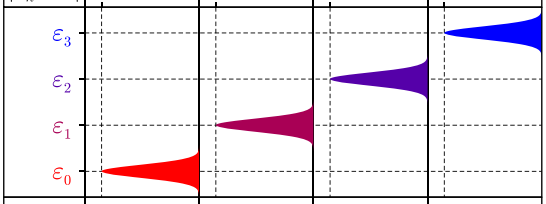			
#paths	1	3	3	1
CGC	1	$\frac{1}{\sqrt{15}}$	$\frac{1}{\sqrt{15}}$	1

Table 2. Same as table 1 for three-photon ionization with O-LP bichromatic femtosecond laser pulses. In the O-LP case, both colors are superpositions of an L-CP and an R-CP field and, vice versa, both helicities exhibit a bichromatic spectrum. Consequently, the $\{a_{nj}\}$ matrix is fully occupied.

(a)

ε_n, $m_j =$	$+3$	$+1$	-1	-3
ε_3	$\frac{1}{3}$	$\frac{1}{\sqrt{15}}$	$\frac{1}{\sqrt{15}}$	$\frac{1}{3}$
ε_2	1	$\frac{1}{\sqrt{15}}$	$-\frac{1}{\sqrt{15}}$	-1
ε_1	1	$-\frac{1}{\sqrt{15}}$	$-\frac{1}{\sqrt{15}}$	1
ε_0	$\frac{1}{3}$	$-\frac{1}{\sqrt{15}}$	$\frac{1}{\sqrt{15}}$	$-\frac{1}{3}$

(b)

m_j	$+3$	$+1$	-1	-3
$\lvert c_n^{(q_1q_2q_3)}\rvert$	1 1/3	1/3	1/3	1 1/3
	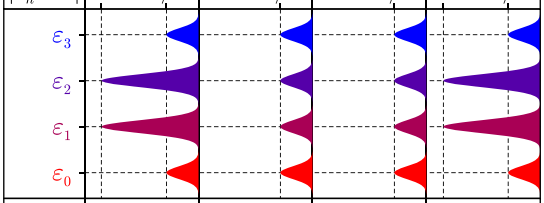			
#paths	1	3	3	1
CGC	1	$\frac{1}{\sqrt{15}}$	$\frac{1}{\sqrt{15}}$	1

corresponding CGCs and, in addition, by the amplitude of the third order spectrum $\tilde{E}^{(3)}_{q_1q_2q_3}(\omega_n)$ evaluated at $\omega_n = \frac{\varepsilon_n + \mathrm{IP}}{\hbar}$. Table 2 gives an overview of all coefficients a_{nj} in the O-LP case.

Finally, we specialize our discussion on a polarization-shaped bichromatic pulse with two spectral bands of identical shape described by a common shape function $\tilde{g}(\omega)$, such that $\tilde{E}^{-}_{q}(\omega) = A_{q,r} \cdot \tilde{g}(\omega - \omega_r) + A_{q,b} \cdot \tilde{g}(\omega - \omega_b)$ with $A_{q,r/b}$ being complex-valued amplitudes. Then, the convolution in equation (3) is readily performed yielding a third order spectrum of the form $E^{(3)}_{q_1q_2q_3}(\omega) = \sum_{n=0}^{3} c_n^{(q_1q_2q_3)} \cdot \tilde{g}^{(3)}(\omega - \omega_n)$. The coefficients $c_n^{(q_1q_2q_3)}$ are functions of the field amplitudes $A_{q,r/b}$ and describe the total amplitudes of the four energy contributions resulting from constructive or destructive interference of all frequency mixing pathways with the same helicity combination $\{q_1q_2q_3\}$. The function $\tilde{g}^{(3)}(\omega) = (\tilde{g} \otimes \tilde{g} \otimes \tilde{g})(\omega)$ is the third order optical spectrum of the spectral shape function. In the CNR-CP case, the weights of all contributions in the third order spectrum are equal (see table 1(b)). In the O-LP case, however, the contributions at ε_1 and ε_2 are reduced to 1/3 for the $m_j = \pm 1$ states due to partial destructive interference of the three individual pathways contributing to the same final state (see table 2(b)). Inserting this result into equation (4) and introducing the energy distribution function $\gamma(\varepsilon) = \tilde{g}^{(3)}(\varepsilon/\hbar)$, the photoelectron wave packet within the nth energy band reads (see equation (1))

$$|\psi_n(\varepsilon)\rangle \propto \gamma(\varepsilon - \varepsilon_n) \sum_{j=0}^{3} a_{nj} |f, m_j\rangle. \tag{5}$$

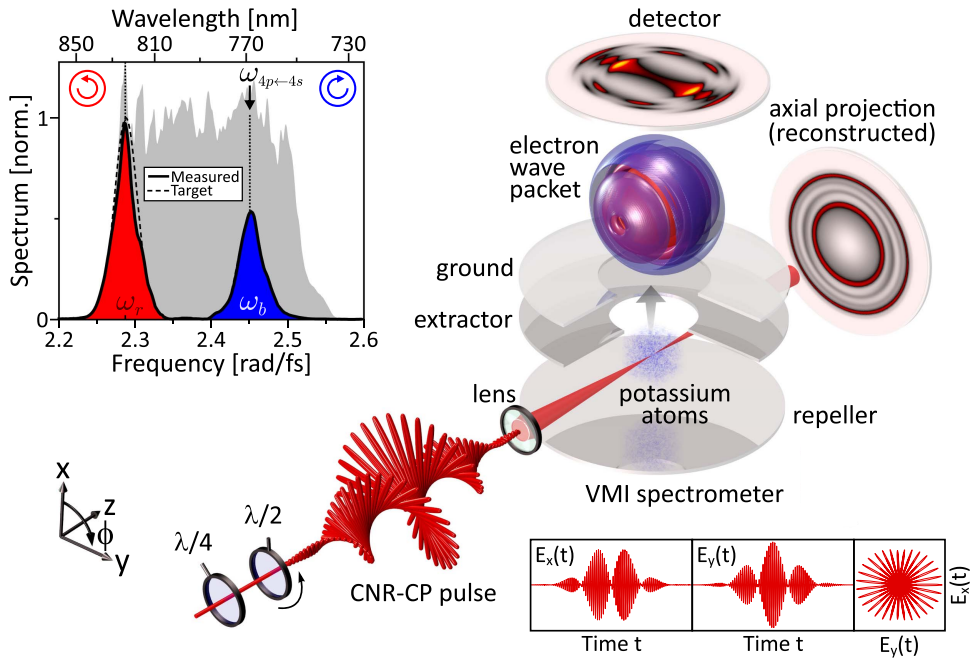

Figure 2. Experimental setup. 3D-EDs from REMPI of potassium atoms with polarization-shaped bichromatic laser pulses are measured using a VMI spectrometer. The laser pulses are rotated by a $\lambda/2$ plate to measure different projections of the electron wave packet and subsequently reconstruct the full 3D information employing a tomographic technique. The shaped laser pulses are generated using a polarization pulse shaper (not shown) equipped with a custom composite polarizer for individual phase and amplitude modulation of two orthogonally polarized spectral bands. For the experiments with CNR-CP pulses, the O-LP output pulses are converted by a $\lambda/4$ plate. The top left inset shows a measured amplitude profile of the bichromatic pulses used in the experiments. The bottom right insets show different projections of the generic CNR-CP pulse.

The weights a_{nj} are given by the products of the coefficients $c_n^{(q_1 q_2 q_3)}$ and the corresponding CGCs, summed over all relevant helicity combinations as described by equation (4). The weighted energy distributions are shown in table 1(b) for the CNR-CP and in table 2(b) for the O-LP case. Finally, we use the spherical harmonics to describe the angular part of the photoelectron wave funtion

$$\psi_n(\varepsilon, \theta, \phi) \propto \gamma(\varepsilon - \varepsilon_n) \sum_{j=0}^{3} a_{nj} \cdot Y_{3,m_j}(\theta, \phi) \tag{6}$$

and obtain the 3D-ED as the probability density of the coherent superposition state

$$\mathcal{P}(\varepsilon, \theta, \phi) \propto \left| \sum_{n=0}^{3} \psi_n(\varepsilon, \theta, \phi) \right|^2 . \tag{7}$$

2.1. Counterrotating circular polarization

The scheme for three-photon ionization with a CNR-CP bichromatic femtosecond laser pulse is depicted in figure 1(b). The spectrum of the ionizing laser field shown in figure 2 has two Gaussian-shaped bands corresponding to two pulses with different central frequencies: a red L-CP laser pulse $\tilde{E}_L^-(\omega)$ centered at ω_r and a blue R-CP pulse $\tilde{E}_R^-(\omega)$ centered at ω_b. If the two pulses coincide in time, the superposition of both colors produces a corkscrew-type temporal polarization profile, as illustrated in figure 2. For larger spectral separation and commensurable center frequencies the polarization profile changes into a characteristic propeller shape [26, 36, 37]. Here, due to the small spectral separation, the propeller leaves are very narrow, resulting in quasi-linear instantaneous polarization slowly rotating with the beating frequency $(\omega_b - \omega_r)/2$. Absorption of three red L-CP photons leads to selective excitation of the $|f, 3\rangle$ free electron wave packet with a toroidal momentum distribution centered at a kinetic energy of $\varepsilon_0 = 3\hbar\omega_r - \mathrm{IP}$ via the $|4s, 0\rangle \xrightarrow{L} |4p, 1\rangle \xrightarrow{L} |d, 2\rangle \xrightarrow{L} |f, 3\rangle$ ionization pathway. Analogously, ionization through the $|4s, 0\rangle \xrightarrow{R} |4p, -1\rangle \xrightarrow{R} |d, -2\rangle \xrightarrow{R} |f, -3\rangle$ pathway creates a torus-shaped free electron wave packet at $\varepsilon_3 = 3\hbar\omega_b - \mathrm{IP}$. Because the electron wave packets from absorption of three red L-CP photons ($|f, 3\rangle$ at $\varepsilon_0 = 3\hbar\omega_r - \mathrm{IP}$) and three blue R-CP photons ($|f, -3\rangle$ at $\varepsilon_3 = 3\hbar\omega_b - \mathrm{IP}$) do not overlap energetically, the resulting photoelectron distribution is a 'torus within a torus'—in contrast to the electron vortex observed by single color REMPI [42]. In addition, if the red and blue

pulses coincide in time, further pathways for ionization are available by frequency mixing. The states at the two intermediate kinetic energies ε_1 and ε_2 are each connected to the ground state via three ionization pathways with different combinations of red L-CP and blue R-CP photons. For example, all three possible pathways for photoionization by absorption of one blue R-CP photon and two red L-CP photons via the pathways $|4s,\,0\rangle \xrightarrow{R} |4p,\,-1\rangle \xrightarrow{L} |d,\,0\rangle \xrightarrow{L} |f,\,1\rangle$, $|4s,\,0\rangle \xrightarrow{L} |4p,\,1\rangle \xrightarrow{R} |d,\,0\rangle \xrightarrow{L} |f,\,1\rangle$ and $|4s,\,0\rangle \xrightarrow{L} |4p,\,1\rangle \xrightarrow{L} |d,\,2\rangle \xrightarrow{R} |f,\,1\rangle$ end in the $|f,\,1\rangle$ continuum state at $\varepsilon_1 = 2\hbar\omega_r + \hbar\omega_b - \mathrm{IP}$. By multiplication of the respective transition amplitudes and coherent addition of all contributions, the relative weight of this ionization pathway is determined to be $a_{11} = \sqrt{3/5}$ (see table 1(a)). Indeed, in both frequency mixing cases the respective three ionization pathways end in a single continuum state, i.e. state $|f,\,1\rangle$ at ε_1 and state $|f,\,-1\rangle$ at ε_2. Ionization with bichromatic CNR-CP fields creates a unique mapping of the angular momentum states $|f,\,m_j\rangle$ to the respective kinetic energy. Therefore, the matrix to describe the state vector at a given kinetic energy of the free electron wave packet $\psi_n(\varepsilon,\,\theta,\,\phi)$ in terms of the angular momentum states $|f,\,m_j\rangle$ described by equation (6) is diagonal for ionization with CNR-CP pulses (see table 1(a)).

2.2. Orthogonal linear polarization

The scheme for excitation and ionization with O-LP bichromatic femtosecond laser pulses is shown in figure 1(c). In the spherical basis both linearly polarized pulses, i.e. the red *s*- and the blue *p*-polarized pulse, are represented by superpositions of an R-CP and an L-CP field. The relative optical phase of $\phi = \pi$ in the R-CP component of the red pulse is introduced to describe the 90° spatial rotation of the red pulse with respect to the blue. This optical phase is imparted on all $\Delta m = -1$ transitions driven by the red pulse. Excitation and ionization with the blue *p*-polarized pulse creates a superposition of all angular momentum states $|f,\,m_j\rangle$ centered at the kinetic energy ε_3. Their weights a_{nj} are given by the sum over all products of the transition amplitudes of all permissible pathways and result in an $|f,\,m = 0\rangle$-type wave packet—briefly termed '*f*-wave' in the following—rotated by 90° about the *x*-axis and aligned along the polarization direction of the blue pulse, i.e. the *y*-axis [39, 41]. The red *s*-polarized pulse ionizes via the same pathways to create an electron wave packet at ε_0. However, the additional relative phase of π rotates the '*f*-wave' by 90° about the *y*-axis. As a result, O-LP ionization creates an '*f*- within an *f*-wave', one of which is rotated with respect to the other. To describe the contributions at ε_1 and ε_2 all permissible frequency mixing pathways (e.g. one blue *p*-polarized photon and two red *s*-polarized photons) are considered and added coherently taking into account the relative phases. The resulting coefficients a_{nj} for photoionization with O-LP pulses presented in table 2(a) show that all superposition states $\psi_n(\varepsilon,\,\theta,\,\phi)$ at the respective energies ε_n have contributions from all angular momentum states $|f,\,m_j\rangle$.

Because the states $|\psi_0(\varepsilon_0)\rangle$ and $|\psi_3(\varepsilon_3)\rangle$ are rotated $|f,\,0\rangle$ states, the amplitudes are also obtained by decomposition into the angular momentum states $|f,\,m_j\rangle$ and thus proportional to the elements of the Wigner *D*-matrices $D^{(3)}_{m_j,0}\left(0,\,\frac{\pi}{2},\,0\right)$ and $D^{(3)}_{m_j,0}\left(\frac{\pi}{2},\,\frac{\pi}{2},\,0\right)$ [41]. The photoelectron distributions at ε_1 and ε_2 are mainly superpositions of the $|f,\,3\rangle$ and $|f,\,-3\rangle$ states with minor contributions from the $|f,\,\pm1\rangle$ states. The alternation of the signs of the coefficients to describe the superposition states $|\psi_1\rangle$ and $|\psi_2\rangle$ at the energies ε_1 and ε_2 shown in table 2, i.e. $a_{2j} = (-1)^{\frac{m_j+1}{2}} a_{1j}$, corresponds to the rotation of the $|\psi_1\rangle$ state by 90° about the *z*-axis in accordance with the drawings shown in the insets (ε_1 and ε_2) to figure 1(c).

3. Experimental

In our experiment, we combine bichromatic polarization pulse shaping with photoelectron imaging in order to create and detect photoelectron wave packets from 1 + 2 REMPI of potassium atoms with CNR-CP and O-LP bichromatic laser pulses. Using tomographic techniques, the full 3D-ED is reconstructed from a series of 2D projections of the wave packets measured under various different angles.

3.1. Bichromatic polarization pulse shaping

Recently, we introduced an optical common-path scheme based on a 4*f* polarization pulse shaper for the generation of polarization-shaped bichromatic laser pulses [36, 37]. The shaper, equipped with a dual-layer liquid crystal spatial light modulator (LC-SLM; Jenoptik, SLM-S640d) for independent amplitude and phase modulation, is employed to sculpture a bichromatic amplitude profile from the spectrum of a 20 fs, 790 nm input pulse provided by a femtosecond laser system (Femtolasers Femtopower HR 3 kHz CEP amplifier seeded by a Rainbow 500 oscillator). A custom composite polarizer consisting of two parts with orthogonal transmission axes (*s*- and *p*-polarized) is mounted in the Fourier plane of the 4*f* setup to enable independent spectral amplitude and phase modulation of two orthogonally polarized spectral bands. Application of the phase functions

$$\varphi_A(\omega) = \begin{cases} \varphi_1(\omega) - \operatorname{acos}\left(\frac{\mathcal{A}_1(\omega)}{\tilde{E}(\omega)}\right), & \omega < \omega_0 \\ \varphi_2(\omega) + \operatorname{acos}\left(\frac{\mathcal{A}_2(\omega)}{\tilde{E}(\omega)}\right), & \omega \geqslant \omega_0 \end{cases} \tag{8}$$

and

$$\varphi_B(\omega) = \begin{cases} \varphi_1(\omega) - \operatorname{acos}\left(-\frac{\mathcal{A}_1(\omega)}{\tilde{E}(\omega)}\right), & \omega < \omega_0 \\ \varphi_2(\omega) - \operatorname{acos}\left(\frac{\mathcal{A}_2(\omega)}{\tilde{E}(\omega)}\right), & \omega \geqslant \omega_0 \end{cases}, \tag{9}$$

with ω_0 denoting the center frequency of the input spectral amplitude $\tilde{E}(\omega)$, to the LC displays A and B of the LC-SLM yields O-LP bichromatic fields with individually adjustable amplitude profiles $\mathcal{A}_{1/2}(\omega)$, phase modulation functions $\varphi_{1/2}(\omega)$, and polarization states (s- or p-polarized) of both colors. Conversion to CNR-CP bichromatic fields is achieved using a quarter wave plate at the shaper output with optical axis aligned at $\pm 45^\circ$ with respect to the x-axis (see figure 2). The inset to figure 2 shows a measured bichromatic spectrum, as used in the experiments, in front of the input spectrum shown as gray-shaded background. For the bichromatic spectrum we used two Gaussian-shaped amplitude profiles $\mathcal{A}_{1/2}(\omega)$ of the same bandwidth $\Delta\omega = 35$ mrad fs^{-1} corresponding to a pulse duration of $\Delta t = 80$ fs. The center frequency of the blue pulse was tuned to the potassium resonance $4p \leftarrow 4s$ at $\omega_b = 2.45$ rad fs^{-1} ($\lambda_b = 769$ nm). The red pulse was centered at $\omega_r = 2.29$ rad fs^{-1} ($\lambda_r = 823$ nm). The amplitude ratio of roughly 2:1 was chosen to match the one-color photoelectron yields of the resonant and the red-detuned pulse (see also section 4). In order to introduce a time delay τ between the two colors with the pulse shaper, we use linear spectral phases

$$\varphi_{1/2}(\omega) = \pm\frac{\tau}{2} \cdot (\omega - \omega_{r/b}), \tag{10}$$

in equations (8) and (9). By applying the linear phases with respect to the center frequencies ω_r and ω_b, only the temporal envelopes of both colors are shifted in time while the respective carriers remain fixed, leaving the relative phase between the colors unaltered. To ensure bandwidth-limited bichromatic output pulses, we compensate the residual spectral phase of the input pulse using the pulse shaper and an evolutionary algorithm to adaptively optimize the second harmonic generation in a β-barium borate crystal [36, 48, 49].

3.2. Photoelectron imaging tomography

The 3D-EDs are measured using photoelectron imaging spectroscopy in combination with a tomographic reconstruction technique described in [39, 41]. As sketched in figure 2, the laser is focused by a 250 mm lens into the interaction region of a VMI spectrometer to interact with potassium vapor (pressure 5×10^{-7} mbar) provided by a dispenser source. The laser intensity used in the experiments was $I_0 \approx 10^{11}$ W cm^{-2}. Photoelectron wave packets released by the laser-atom interaction are imaged onto a multi-channel plate detector in chevron configuration stacked with a phosphor screen. About two events per laser pulse were detected on the screen. Images of the screen are recorded by a CCD camera with an exposure time of 250 ms. Each projected electron momentum distribution (PED) was recorded by accumulation of 400 images. The energy resolution of the PEDs is better than 80 meV at 1 eV. In general, 3D-EDs from photoionization with polarization-shaped laser pulses exhibit no rotational symmetry, precluding a reconstruction by Abel inversion. By rotating the incident laser pulses using a $\lambda/2$ wave plate, we measured PEDs under 31 angles from 0° to 90°. From the recorded 2D PEDs the 3D-EDs were reconstructed using the Fourier slice algorithm [50]. The Fourier-based algorithm described in [39] is specifically adapted to the reconstruction in spherical coordinates and was found to be better suited than the back projection algorithm.

4. Results and discussion

In this section, we present measured free electron wave packets from REMPI of potassium atoms by CNR-CP (section 4.1) and O-LP (section 4.2) bichromatic pulses.

4.1. Counterrotating circular polarization

Figure 3(a) shows sections through the tomographically reconstructed 3D-EDs from CNR-CP ionization. The data shown in different columns corresponds to three different time delays τ. Different rows represent the three cartesian principal planes. For $\tau = 0$ (middle column) both colors coincide in time. The respective sections exhibit four contributions centered around momenta $p_n = \sqrt{2m_e\varepsilon_n}$, with m_e denoting the electron mass and ε_n being the central energy of the nth energy window as introduced in section 2. For best visibility, the weaker p_1- and p_2-contribution were enhanced by factors of 4.7 and 3.1, respectively. The right half of each section shows

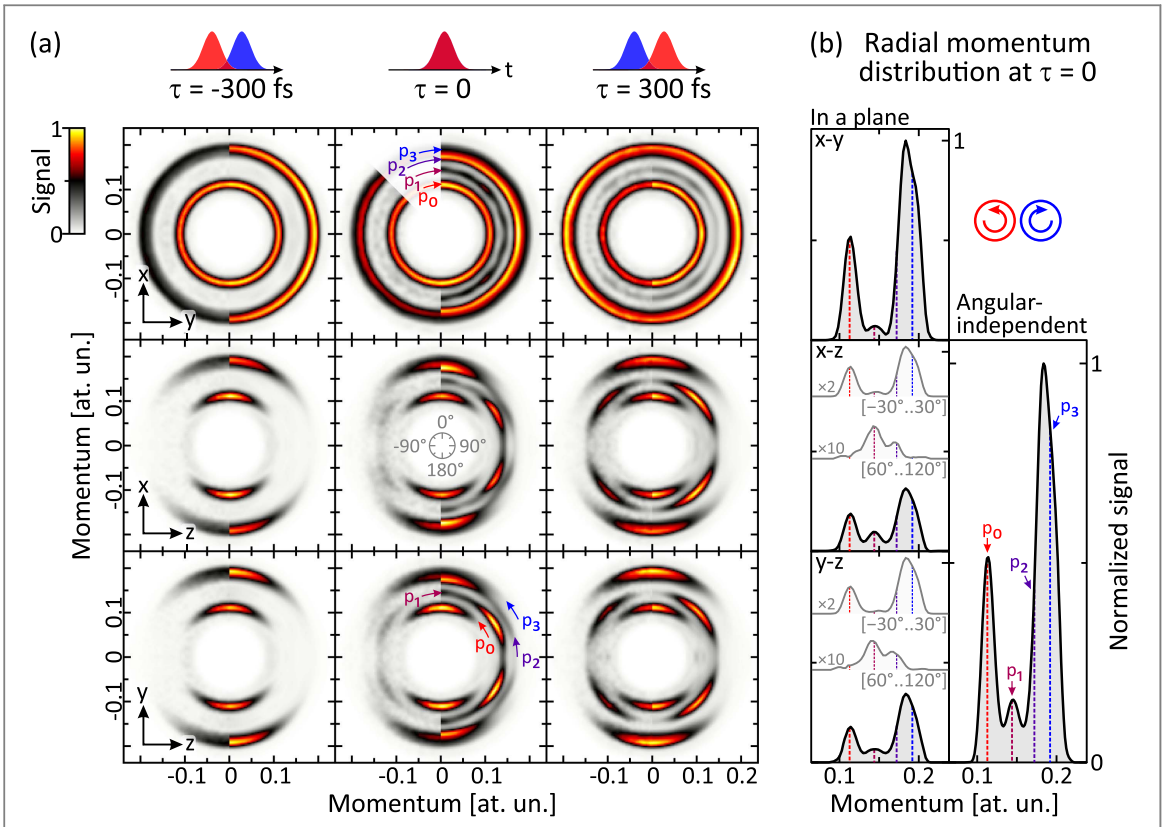

Figure 3. (a) Sections through the reconstructed 3D-EDs from CNR-CP ionization for three different time delays τ. Positive values of τ indicate that the resonant pulse precedes the red-detuned pulse. Different rows correspond to the three cartesian principal planes. The left half of each section shows the original reconstructed data. In the right half, weak features were enhanced for better visibility. The similarity of the sections in the x–z-plane (middle row) and the y–z-plane (lower row) for all time delays indicates the 3D-ED's rotational symmetry about the z-axis. (b) Angle-integrated spectra of the original data at $\tau = 0$ for assignment of the four energy bands and their relative intensities. The red, magenta, purple, and blue arrows mark the momenta $p_0 \ldots p_3$ corresponding to energies $\varepsilon_0 \ldots \varepsilon_3$.

the enhanced data, while the original reconstructed data is displayed in the left half for comparison. Contributions from one-color multi-photon ionization by the red and blue components are visible at momenta p_0 (red arrow) and p_3 (blue arrow). The circularly symmetric signals in the x–y-plane and the crescent-shaped signals in both the x–z- and the y–z-plane indicate a toroidal shape of the corresponding wave packets, in accordance with the photoelectron states $|\psi_0\rangle \propto |f, 3\rangle$ and $|\psi_3\rangle \propto |f, -3\rangle$ predicted by equation (1) and table 1. In addition, two mixing terms, corresponding to the absorption of either two red and one blue or one red and two blue photons, are visible around p_1 (purple arrow) and p_2 (magenta arrow). While their contribution is likewise circularly symmetric in the x–y-plane, their angular distribution in the x–z- and the y–z-plane exhibits three distinct lobes in the upper and lower hemisphere, reflecting the spherical harmonics $Y_{3,\pm1}(\theta, \phi)$ associated with states $|\psi_1\rangle \propto |f, 1\rangle$ and $|\psi_2\rangle \propto |f, -1\rangle$.

The angular-integrated plots showing the photoelectron distribution as a function of the momentum in a given plane and the angular-independent momentum distribution are displayed in figure 3(b). It is clearly seen that the 2D distributions in (a) allow to discern features which are unresolved in the angular-independent momentum distribution. Even higher differential information is obtained by integration over the angular segments between [–30°..30°] and [60°..120°] in the planar momentum distribution. The resulting differential photoelectron spectra, displayed in the respective insets, highlight the contributions at p_0 and p_3 (in [–30°..30°]) as well as p_1 and p_2 (in [60°..120°]).

Next, we introduce a time delay between the two pulses in the CNR-CP sequence. Separating both colors in time provides an additional check to discriminate different contributions in the photoelectron spectrum. At a time delay of $\tau = -300$ fs (left column of figure 3(a)) the red component precedes the blue. In this case, only the p_0- and p_3-contribution are observed in the photoelectron spectrum, confirming the one-color character of these signals. In contrast, for reversed pulse ordering at $\tau = 300$ fs (right column), the term around p_1 persists. Since the blue band is resonant with the potassium $4p \leftarrow 4s$ transition, excitation by the blue prepulse generates population in the $4p$ state. After time τ the excited system is probed by the red postpulse in a non-resonant two-photon ionization step. Similar to the $\tau = 0$ case, the corresponding wave packet detected around p_1 exhibits

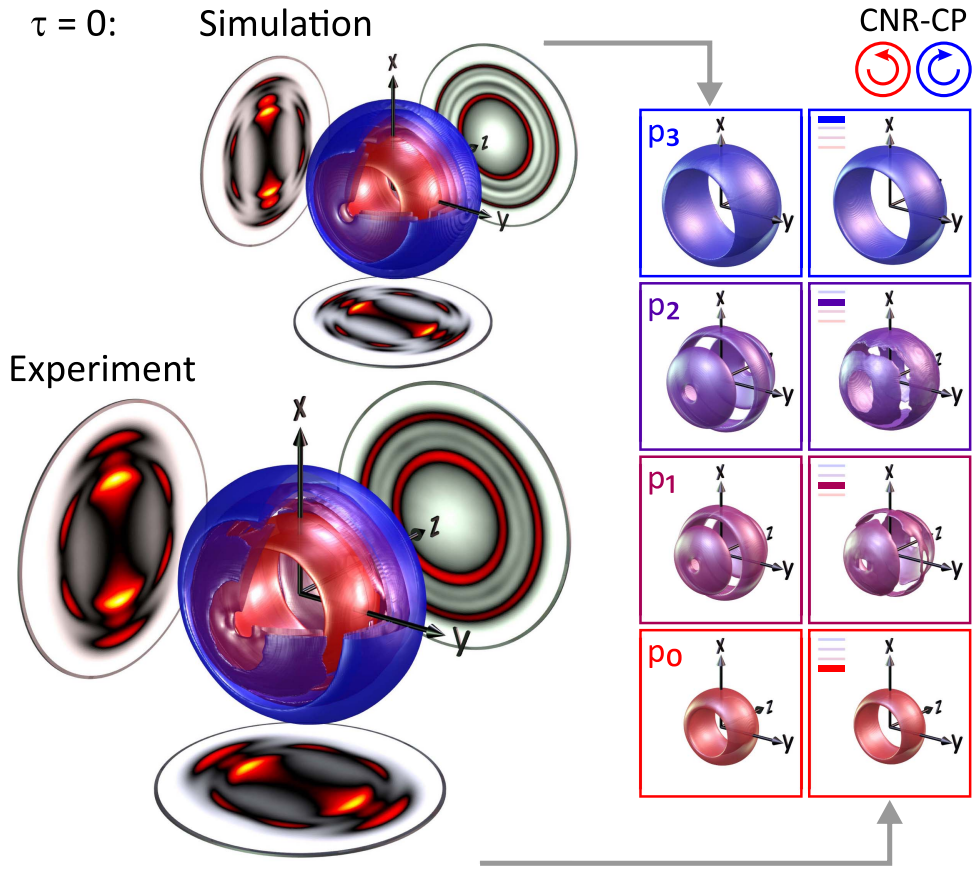

Figure 4. Measured 3D-ED from REMPI with CNR-CP bichromatic pulses for $\tau = 0$. The inset shows the result of a numerical simulation. On the right-hand side, the contributions from the four different frequency mixing ionization pathways are compared side-by-side.

circular symmetry in the *x*–*y*-plane. However, the contributions in the *x*–*z*- and *y*–*z*-plane reveal that the symmetry of the wave packet has changed from three to two lobes in each hemisphere. This delay-dependent shape of the wave packet's angular distribution is due to the time evolution of a SOWP launched by coherent excitation of the two fine structure components $4p_{1/2}$ and $4p_{3/2}$. The chosen time delay roughly corresponds to half the SOWP oscillation period of 578 fs [51, 52]. Note that the SOWP dynamics are captured exclusively by the p_1-contribution. Both one-color ionization pathways are insensitive to the time delay and the p_2-mixing term vanishes with the temporal separation of the two colors. This example of REMPI with bichromatic CNR-CP pulses shows that the energetic disentanglement of the different ionization pathways reveals neutral system dynamics which may be concealed otherwise due to overlapping contributions. A detailed investigation of the SOWP dynamics utilizing shaper-generated polarization-tailored bichromatic pulses in a two-color pump-probe experiment will be presented in a forthcoming publication.

The 3D-EDs presented in figure 4 highlight the excellent agreement of the measured and simulated photoelectron angular distributions for CNR-CP ionization. Separating the photoelectron distributions in the spherical shells containing narrow energy intervals around p_0 to p_3 (insets to figure 4)—much like peeling an onion—permits selective inspection of all four angular momentum states $|f, m_j\rangle$.

4.2. Orthogonal linear polarizations

The reconstructed 3D-ED created by ionization with O-LP pulses at $\tau = 0$ fs is shown in figure 6. Sections through the 3D distributions at $\tau = 0$ fs and $\tau = \pm 300$ fs are depicted in figure 5(a). Weak contributions were enhanced for better visibility using enhancement factors up to 3.9. At $\tau = 0$ fs (middle column) we observe contributions from all four frequency mixing pathways. The outermost contribution at p_3, resulting from one-color ionization by the blue pulse, exhibits an $|f, 0\rangle$-type shape in the *x*–*y*-plane (upper row). Due to the *p*-polarization of the blue band, the two main lobes of the signal are aligned horizontally along the *y*-axis. Consequently, the signal vanishes in the *x*–*z*-plane (middle row) being a nodal plane of the '*f*-wave'. The same symmetry is observed for the innermost contribution at p_0 resulting from one-color ionization by the red pulse. However, due to the *s*-polarization of the red band the corresponding photoelectron signal is aligned vertically

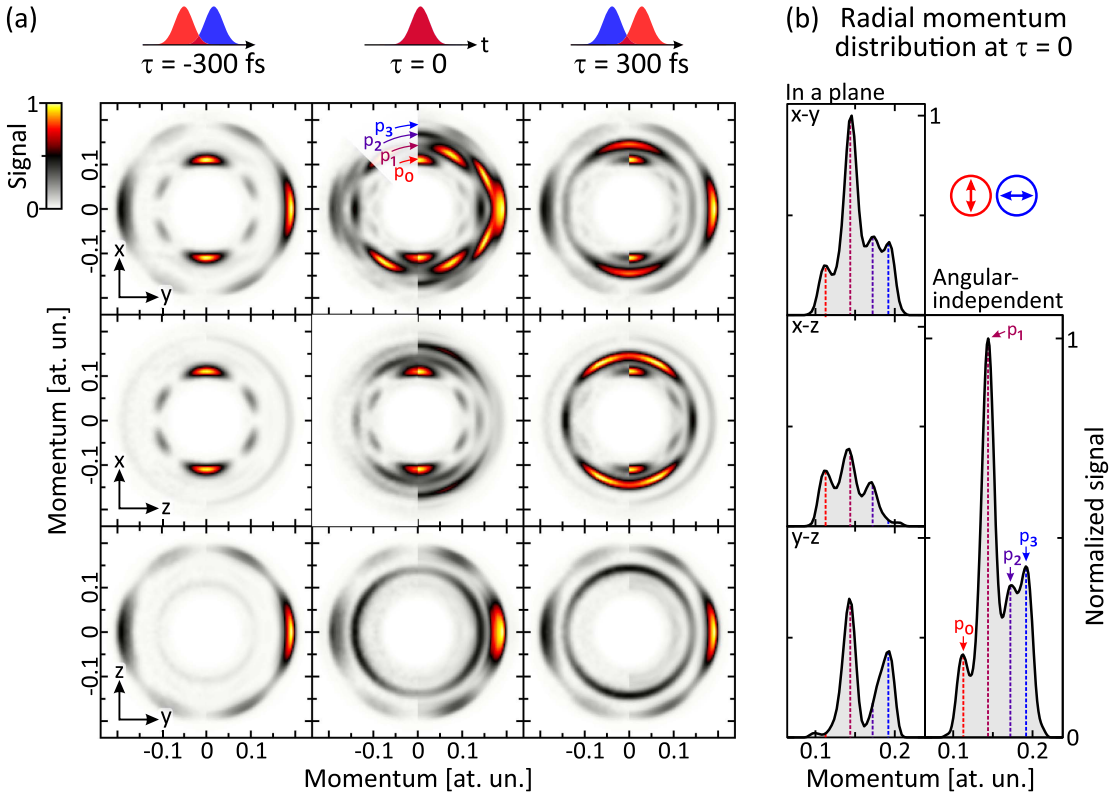

Figure 5. Same as figure 3 for ionization with O-LP bichromatic laser pulses. The similarity of the innermost contribution in the sections in the x–y-plane (upper row) and the x–z-plane (middle row) for all delay times indicates the rotational symmetry of the 3D-ED at p_0 about the x-axis. Rotational symmetry of the outermost contribution about the y-axis is suggested by the similarity of the sections at p_3 in the x–y-plane (upper row) and the y–z-plane (lower row).

along the x-axis and has—due to the rotational symmetry about the x-axis—similar contributions in both the x–y- and the x–z-planes. The symmetry of the two mixing terms is distinctly different. The first mixing term at p_1 exhibits six lobes in the x–y-plane distributed equidistantly in angular intervals of 60°, with the two weakest lobes aligned in opposite directions along the y-axis. The same structure, albeit less pronounced, appears in the x–z-plane, indicating a preferential alignment of the wave packet in the laser polarization plane (x–y-plane). This observation is in agreement with the generic wave packet shown in the inset to figure 1(c) (ε_1-frame) and the discussion in section 2.2, where the six-lobe structure was rationalized to arise from a coherent superposition dominated by the states $|f, \pm 3\rangle$. A similar structure is observed for the p_2-mixing term. In this case however, the two weak lobes in the x–y-plane are aligned along the x-axis. In the x–z-plane only two crescent-shaped signals are observed. Both observations suggest a 90° rotation of the p_2-wave packet relative to the p_1-wave packet about the laser propagation direction (z-axis), as discussed in section 2.2.

By introducing a time delay of $\tau = -300$ fs (left column) only the one-color contributions around p_0 and p_3 remain, while the two mixing terms vanish from the photoelectron spectrum. For the reversed ordering of colors (right column), a pronounced signal is observed around p_2 resulting from resonant excitation and time-delayed probing of the atom. As in the CNR-CP case discussed in the previous section, the angular distribution of the p_1-wave packet evolves in time due to the spin–orbit interaction in the excited $4p$ state. As a result, the contributions in the x–y- and the x–z-plane exchange their roles between $\tau = 0$ and 300 fs, indicating a 90° rotation of the wave packet about the x-axis. This observation shows again that subtle details of the neutral dynamics are revealed by bichromatic REMPI due to the background-free detection of the relevant two-color signal.

The 'f- within an f-wave' along with the two frequency mixing contributions discussed in section 2.2 are clearly observed in the experimental 3D-ED and the simulation shown in figure 6. By isolating the photoelectron distributions belonging to different energy shells around p_0 to p_3, we compare simulated and measured contributions individually (see insets to figure 6) to find excellent agreement, although the equatorial node in the reconstructed p_2-wave packet is not fully resolved due to the energetic overlap with the neighboring lobe of the p_3-wave packet.

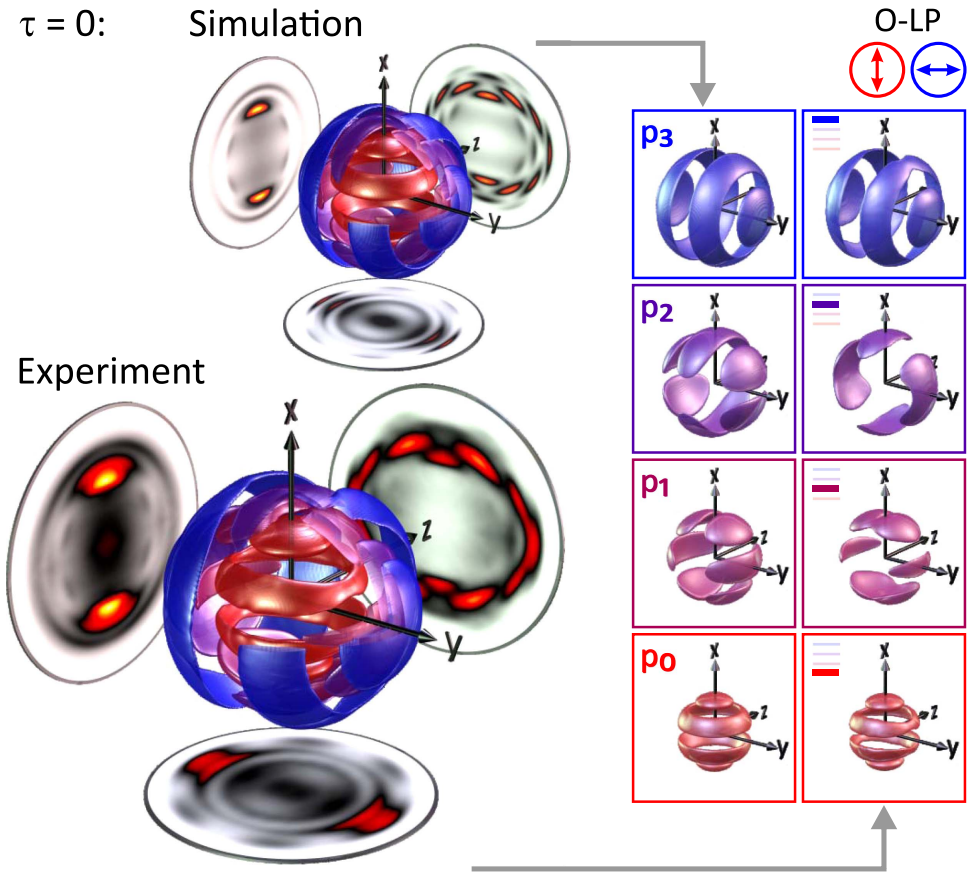

Figure 6. Same as figure 4 for REMPI with O-LP bichromatic pulses and $\tau = 0$. Note that the node of the measured p_2-wave packet (purple) in the y–z-plane is not resolved due to the energetic overlap with the intense main-lobe of the p_3-wave packet (blue).

5. Conclusion

In this paper, we presented the first application of shaper-based polarization-tailored bichromatic femtosecond laser fields to the generation of controlled 3D free electron wave packets. Specifically, we reported on control of 3D-EDs from REMPI of potassium atoms by CNR-CP and O-LP bichromatic laser pulses. In the experiment, bichromatic laser fields consisting of two spectral bands with different ellipticity have been produced using an ultrafast polarization pulse shaper equipped with a custom polarizer in the Fourier plane. Photoelectron momentum images from ionization with CNR-CP and O-LP bichromatic laser pulses have been measured employing a VMI spectrometer. The 3D-EDs have been reconstructed from numerous VMI images using a tomographic algorithm. Our results showed that bichromatic $1 + 2$ REMPI produces photoelectron wave packets with kinetic energies within four distinct energy bands. Both outermost 3D-EDs, at maximum and minimum kinetic energy, originate from one-color ionization respectively, whereas the contributions in between are created by frequency mixing of pulses with different ellipticity. By analyzing the pathways for multi-photon ionization with bichromatic CNR-CP and O-LP pulses, we could accurately characterize the angular quantum states of the observed free electron wave packets. We found that ionization with bichromatic CNR-CP fields creates a unique mapping of the angular momentum states $|f, m_j\rangle$ to the respective kinetic energy bands, permitting selective detection of all four angular momentum states $|f, m_j\rangle$. The two one-color contributions create a 'torus within a torus' and two additional wave packets are generated by frequency mixing. In contrast, bichromatic O-LP laser pulses created four different superposition states, including the 'f- within an f-wave' and two uncommon angular momentum superposition states. By introducing a time delay between the two pulses of different color and ellipticity, the non-resonant frequency mixing contribution vanished, whereas the resonant part persisted when the resonant excitation pulse preceded the off-resonant ionization pulse. Besides the discrimination of resonant and non-resonant ionization pathways, bichromatic excitation enabled background-free detection of a SOWP in one specific photoelectron kinetic energy band.

In this contribution, REMPI of atoms with bichromatic CNR-CP and O-LP pulses served as a model system to demonstrate the extraction of detailed information on neutral dynamics and control of multi-photon ionization pathways. Our analysis of the 3D-EDs showed that the physical mechanism of control by bichromatic

polarization-shaped fields is based on the interplay of photoionization pathway selection by the ellipticity of the pulses and intrapulse frequency mixing of the spectral bands with different ellipticity.

In general, shaper-based creation of bichromatic polarization-tailored fields is a powerful experimental technique to study and manipulate the dynamics of quantum systems because it combines the advantages of polarization shaping, i.e. control of the 3D nature of the light–matter interaction, with the spectroscopic characteristics of bichromatic control. Currently we perform two-color polarization-sensitive pump-probe experiments using bichromatic polarization-shaped pulses to investigate spin–orbit and Rydberg wave packet dynamics and to perform time-resolved studies of the photoelectron circular dichroism of chiral molecules.

Acknowledgments

Financial support by the Deutsche Forschungsgemeinschaft via the priority programme SPP1840 QUTIF is gratefully acknowledged.

References

[1] Brixner T and Gerber G 2001 Femtosecond polarization pulse shaping *Opt. Lett.* **26** 557–9
[2] Brixner T, Krampert G, Niklaus P and Gerber G 2002 Generation and characterization of polarization-shaped femtosecond laser pulses *Appl. Phys.* B **74** s133–44
[3] Wollenhaupt M, Krug M, Köhler J, Bayer T, Sarpe-Tudoran C and Baumert T 2009 Photoelectron angular distributions from strong-field coherent electronic excitation *Appl. Phys.* B **95** 245–59
[4] Wollenhaupt M, Bayer T and Baumert T 2015 *Control of Ultrafast Electron Dynamics with Shaped Femtosecond Laser Pulses: From Atoms to Solids* (Berlin: Springer) pp 63–122 book section 4
[5] Misawa K 2016 Applications of polarization-shaped femtosecond laser pulses *Adv. Phys.* X **1** 544–69
[6] Dudovich N, Oron D and Silberberg Y 2004 Quantum control of the angular momentum distribution in multiphoton absorption processes *Phys. Rev. Lett.* **92** 103003
[7] Brixner T, Krampert G, Pfeifer T, Selle R, Gerber G, Wollenhaupt M, Graefe O, Horn C, Liese D and Baumert T 2004 Quantum control by ultrafast polarization shaping *Phys. Rev. Lett.* **92** 208301
[8] Hockett P, Wollenhaupt M, Lux C and Baumert T 2014 Complete photoionization experiments via ultra-fast coherent control with polarization-multiplexing *Phys. Rev. Lett.* **112** 223001
[9] Shafir D, Mairesse Y, Villeneuve D M, Corkum P B and Dudovich N 2009 Atomic wavefunctions probed through strong-field light–matter interaction *Nat. Phys.* **1251** 412 –416
[10] Xie X H *et al* 2013 Probing the influence of the Coulomb field on atomic ionization by sculpted two-color laser fields *New J. Phys.* **15** 043050
[11] Zhang L *et al* 2014 Subcycle control of electron–electron correlation in double ionization *Phys. Rev. Lett.* **112** 193002
[12] Richter M, Kunitski M, Schöffler M, Jahnke T, Schmidt L P H, Li M, Liu Y Q and Dörner R 2015 Streaking temporal double-slit interference by an orthogonal two-color laser field *Phys. Rev. Lett.* **114** 143001
[13] Mancuso C A *et al* 2015 Strong-field ionization with two-color circularly polarized laser fields *Phys. Rev.* A **91** 031402
[14] Thompson M R, Thomas M K, Taday P F, Posthumus J H, Langley A J, Frasinski L J and Codling K 1997 One and two-colour studies of the dissociative ionization and Coulomb explosion of h_2 with intense ti:sapphire laser pulses *J. Phys. B: At. Mol. Opt. Phys.* **30** 5755
[15] Ray D *et al* 2009 Ion-energy dependence of asymmetric dissociation of d-2 by a two-color laser field *Phys. Rev. Lett.* **103** 223201
[16] Dupont E, Corkum P B, Liu H C, Buchanan M and Wasilewski Z R 1995 Phase-controlled currents in semiconductors *Phys. Rev. Lett.* **74** 3596–9
[17] Costa L, Betz M, Spasenovic M, Bristow A D and Van Driel H M 2007 All-optical injection of ballistic electrical currents in unbiased silicon *Nat. Phys.* **3** 632–5
[18] Güdde J, Rohleder M, Meier T, Koch S W and Höfer U 2007 Controlled electric currents at a metal surface time-resolved investigation of coherently *Science* **318** 1287–91
[19] Long S, Becker W and McIver J K 1995 Model calculations of polarization-dependent two-color high-harmonic generation *Phys. Rev.* A **52** 2262–78
[20] Eichmann H, Egbert A, Nolte S, Momma C, Wellegehausen B, Becker W, Long S and McIver K 1995 Polarization-dependent high-order two-color mixing *Phys. Rev.* A **51** R3414–7
[21] Dudovich N, Smirnova O, Levesque J, Mairesse Y, Ivanov M Y, Villeneuve D M and Corkum P B 2006 Measuring and controlling the birth of attosecond XUV pulses *Nat. Phys.* **2** 781–6
[22] Corkum P B, Burnett N H and Ivanov M Y 1994 Subfemtosecond pulses *Opt. Lett.* **19** 1870–2
[23] Kitzler M and Lezius M 2005 Spatial control of recollision wave packets with attosecond precision *Phys. Rev. Lett.* **95** 253001
[24] Feng X, Gilbertson S, Mashiko H, Wang H, Khan S D, Chini M, Wu Y, Zhao K and Chang Z 2009 Generation of isolated attosecond pulses with 20 to 28 femtosecond lasers *Phys. Rev. Lett.* **103** 183901
[25] Brugnera L, Hoffmann D J, Siegel T, Frank F, Zair A, Tisch J W G and Marangos J P 2011 Trajectory selection in high harmonic generation by controlling the phase between orthogonal two-color fields *Phys. Rev. Lett.* **107** 153902
[26] Milosevic D B, Becker W and Kopold R 2000 Generation of circularly polarized high-order harmonics by two-color coplanar field mixing *Phys. Rev.* A **61** 063403
[27] Milosevic D B and Becker W 2000 Attosecond pulse trains with unusual nonlinear polarization *Phys. Rev.* A **62** 011403
[28] Fleischer A, Kfir O, Diskin T, Sidorenko P and Cohen O 2014 Spin angular momentum and tunable polarization in high-harmonic generation *Nat. Photon.* **8** 543–9
[29] Kfir O *et al* 2015 Generation of bright phase-matched circularly-polarized extreme ultraviolet high harmonics *Nat. Photon.* **9** 99–105
[30] Fan T T *et al* 2015 Bright circularly polarized soft x-ray high harmonics for x-ray magnetic circular dichroism *Proc. Natl Acad. Sci.* **112** 14206–11
[31] Yuan K J and Bandrauk A D 2015 Attosecond-magnetic-field-pulse generation by electronic currents in bichromatic circularly polarized UV laser fields *Phys. Rev.* A **92** 063401

[32] Mauger F, Bandrauk A D and Uzer T 2016 Circularly polarized molecular high harmonic generation using a bicircular laser *J. Phys. B: At. Mol. Opt. Phys.* **49** 10LT01
[33] Baykusheva D, Ahsan M S, Lin N and Wörner H J 2016 Bicircular high-harmonic spectroscopy reveals dynamical symmetries of atoms and molecules *Phys. Rev. Lett.* **116** 123001
[34] Reich D M and Madsen L B 2016 Illuminating molecular symmetries with bicircular high-order-harmonic generation *Phys. Rev. Lett.* **117** 133902
[35] Weiner A M 2000 Femtosecond pulse shaping using spatial light modulators *Rev. Sci. Instrum.* **71** 1929–60
[36] Kerbstadt S, Englert L, Bayer T and Wollenhaupt M 2017 Ultrashort polarization-tailored bichromatic fields *J. Mod. Opt.* **64** 1010
[37] Kerbstadt S, Timmer D, Englert L, Bayer T and Wollenhaupt M 2017 Ultrashort polarization-tailored bichromatic fields from a cep-stable white light supercontinuum *Opt. Express* **25** 12518
[38] Eppink A T J B and Parker D H 1997 Velocity map imaging of ions and electrons using electrostatic lenses: application in photoelectron and photofragment ion imaging of molecular oxygen *Rev. Sci. Instrum.* **68** 3477–84
[39] Wollenhaupt M, Krug M, Köhler J, Bayer T, Sarpe-Tudoran C and Baumert T 2009 Three-dimensional tomographic reconstruction of ultrashort free electron wave packets *Appl. Phys.* B **95** 647–51
[40] Smeenk C, Arissian L, Staude A, Villeneuve D M and Corkum P B 2009 Momentum space tomographic imaging of photoelectrons *J. Phys. B: At. Mol. Opt. Phys.* **42** 185402
[41] Wollenhaupt M, Lux C, Krug M and Baumert T 2013 Tomographic reconstruction of designer free-electron wave packets *Chem. Phys. Chem.* **14** 1341–9
[42] Pengel D, Kerbstadt S, Johannmeyer D, Englert L, Bayer T and Wollenhaupt M 2017 Electron vortices in femtosecond multiphoton ionization *Phys. Rev. Lett.* **118** 053003
[43] Hockett P, Wollenhaupt M and Baumert T 2015 Coherent control of photoelectron wavepacket angular interferograms *J. Phys. B: At. Mol. Opt. Phys.* **48** 214004
[44] Dudovich N, Dayan B, Gallagher Faeder S M and Silberberg Y 2001 Transform-limited pulses are not optimal for resonant multiphoton transitions *Phys. Rev. Lett.* **86** 47–50
[45] Wollenhaupt M, Präkelt A, Sarpe-Tudoran C, Liese D, Bayer T and Baumert T 2006 Femtosecond strong-field quantum control with sinusoidally phase-modulated pulses *Phys. Rev.* A **73** 063409
[46] Gandman A, Chuntonov L, Rybak L and Amitay Z 2007 Coherent phase control of resonance-mediated (2+1) three-photon absorption *Phys. Rev.* A **75** 031401
[47] Meshulach D and Silberberg Y 1999 Coherent quantum control of multiphoton transitions by shaped ultrashort optical pulses *Phys. Rev.* A **60** 1287–92
[48] Baumert T, Brixner T, Seyfried V, Strehle M and Gerber G 1997 Femtosecond pulse shaping by an evolutionary algorithm with feedback *Appl. Phys.* B **65** 779–82
[49] Yelin D, Meshulach D and Silberberg Y 1997 Adaptive femtosecond pulse compression *Opt. Lett.* **22** 1793–5
[50] Kak A C and Slaney M 1988 *Principles of Computerized Tomographic Imaging* (New York: IEEE Press)
[51] Nicole C, Bouchene M A, Zamith S, Melikechi N and Girard B 1999 Saturation of wave-packet interferences: direct observation of spin precession in potassium atoms *Phys. Rev.* A **60** R1755–8
[52] Braun H, Bayer T, Pengel D, Wollenhaupt M and Baumert T 2017 Simultaneous observation of transient and final state dynamics in ultrafast strong-field excitation via time-resolved photoelectron spectroscopy *J. Mod. Opt.* **64** 1042–53